TRMC using planar microwave resonators: Application to the study of long-lived charge pairs in photoexcited titania nanotube arrays

M. H. Zarifi,[1] A. Mohammadpour,[1] S. Farsinezhad,[1] B. D. Wiltshire,[1] M. Nosrati,[1] A. M. Askar,[1] M. Daneshmand[1] and K. Shankar[1, 2]

[1]*Department of Electrical and Computer Engineering, University of Alberta, Edmonton, Alberta, T6G 2V4, Canada*

[2]*National Institute for Nanotechnology, National Research Council, Edmonton, Alberta, T6G 2M9, Canada*

Steady-state (SRMC) and time-resolved microwave photoconductivity (TRMC) are key techniques used to perform the contact-less determination of carrier density, transport, trapping and recombination parameters in charge transport materials such as organic semiconductors and dyes, inorganic semiconductors and metal-insulator composites which find use in conductive inks, thin film transistors, light emitting diodes, photocatalysts and photovoltaics. We present the theory, design, simulation and fabrication of a planar microwave ring resonator operating at 5.25 GHz with a quality factor of 224, to perform SRMC and TRMC measurements. Our method consists of measuring the resonance frequency (f_0) and Q-factor of the microwave resonator with the sample to be probed placed in a defined sensitive region of the resonator where the microwave field is highly concentrated. We also provide proof of concept measurements of the time-resolved microwave photoresponse of anatase-phase TiO_2 nanotube array membranes (TNTAMs) using the planar microstrip resonator. An unusual observation was the persistence of charged pair states in TNTAMs for several hours at room temperature under ambient conditions. Fast (120-220 s), slow (1300-2850 s) and very slow (6-26 hrs) components were extracted from the long-lived photoconductive decays of TNTAMs in response to 365 nm, 250 nm and 405 nm illumination, and assigned to various trap-mediated processes in TiO_2 nanotubes.

KEYWORDS: Recombination, Charged Pair Lifetimes, Photodielectric Effect, Complex Permittivity, Deep Traps

Introduction

TRMC has been employed to study the transfer, transport, recombination and trapping of photogenerated charges in organic dyes, conjugated polymers, inorganic nanocrystal quantum dots, and semiconductor single crystals, thin films and nanostructures in devices such as bulk heterojunction solar cells, organic light emitting diodes and photocatalysts.[1-7] The instrumental configuration used most commonly has changed little since the late 1980s and measures reflected microwave power in a resonant cavity waveguide, typically in the X-band, using an experimental configuration depicted in Figure 1.[1, 4, 8-10] Cavity waveguides are bulky and need careful tuning of the resonant dimensions to adjust the spatial location of the standing wave nodes. The planar microwave resonator configuration forms a superior alternative to cavity waveguides is because it is easier to fabricate, constitutes a monolithic configuration with a small form factor that can be integrated with active circuitry and potentially provides a smaller and lower cost sensor package. It is also generally easier to communicate with microstrip based devices compared to waveguides, and the readout circuitry will be lower cost. Furthermore, membranes made of uniaxial materials can be mounted both edge-wise and flat in the coupling gap to obtain information about their anisotropic permittivities.

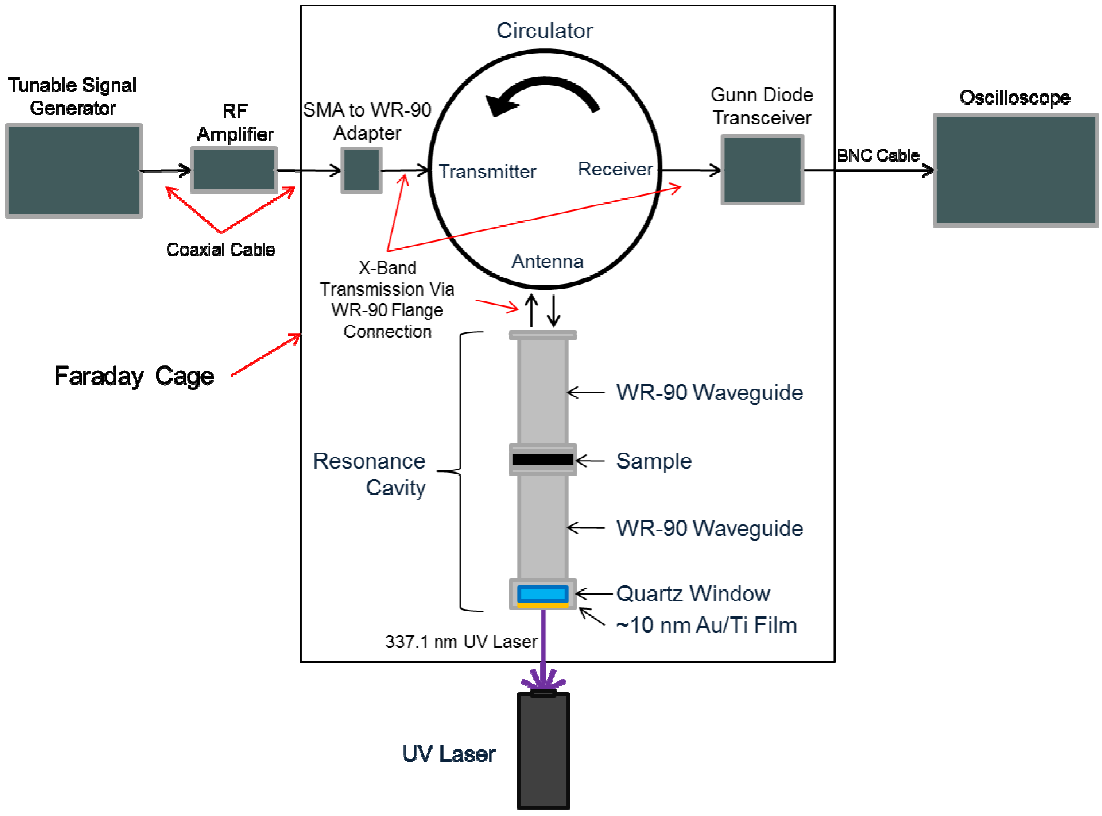

Figure 1. Commonly used cavity waveguide resonator configuration used to perform TRMC measurements

Free carriers in semiconductors strongly absorb microwave radiation in accordance with the Drude-Zener[11] or Drude-Smith relations,[12] and upon irradiation, their contributions to the relative change in microwave power dominate in comparison to the much less mobile impurity ions, dipoles and trapped species. Therefore, the relative change in microwave power ($\Delta P/P$) as a function of time due to injection of excess carriers may be expressed as[13]

$$\frac{\Delta P(t)}{P} = A(\omega) \cdot \Delta\sigma(t) = A(\omega) e\left(\Delta n(t)\mu_n + \Delta p(t)\mu_p\right) \quad (1)$$

where A is a time-independent constant of proportionality, $\Delta n(t)$ and $\Delta p(t)$ are the time-varying excess concentrations of electrons and holes respectively, and μ_n and μ_p are the mobilities of electrons and holes respectively. At the same time, bound charges increase the permittivity of the semiconductor at microwave frequencies due to the photodielectric effect. Steady-state microwave conductivity has been used to estimate the effective mass and momentum relaxation time in semiconductors.[14] Time-resolved microwave conductivity (TRMC) can be thought of as a pump-probe technique in which illumination by band-gap photons is the pump and microwaves to measure carrier dynamics is the probe.[15-17] Planar microwave resonators are compact, portable, rugged and compatible with complementary metal oxide semiconductor (CMOS) integrated circuits. The input and the output signals are coupled to the resonator through two microstrip feed lines, and the capacitive coupling between them and the primary open loop ring microstrip resonator. The resonance frequency (f_0) is determined by the length of the microstrip line and the material properties of the resonator's substrate. Capacitive coupling determines the ring resonator matching, loading and bandwidth which in return affects the signal amplitude, resonance frequency and the quality factor. For measurements of the complex photoconductive decay, we monitor the shift in f_0 and Q in response to light excitation, as a function of time. Both the real and imaginary parts of the electrical permittivity (and therefore the complex conductivity) of the material in the coupling gap can be extracted by measuring two of the following parameters of a microwave signal: amplitude, frequency and the quality factor.[18] These parameters are simply extractable from S-parameters of the microwave resonator. Planar resonators do not require circulators or resonant cavities, and very little customization to measure different types of materials.

TiO_2 nanotube arrays grown by electrochemical anodization are a self-organized, semiconducting nanomaterial whose potential utility in solar fuel generation,[19] photocatalytic water

remediation,[20] low cost photovoltaics,[21] high sensitivity photoelectrochemical sensing[22] and ultrahigh sensitivity resistive gas sensing[23] has been demonstrated in numerous reports. The dynamics of charge carriers play a key role in each of the aforementioned devices. While carrier dynamics in anatase nanoparticles (NPs) have been studied extensively, ordered anatase nanotubes are only recently beginning to receive similar attention and initial studies suggest the trap distribution to be significantly different from NPs.[24-26] In addition, electrons in TiO_2 have been shown to exhibit non-ideal thermodynamic behavior and exciton-like trap states.[27-28] For these reasons, TiO_2 nanotube arrays constitute an interesting platform for microwave conductance measurements. In addition, TiO_2 nanotube array films and membranes are being actively researched for resistive gas sensor and photoconductive UV sensor applications, as well as for the photocatalytic reduction of diluted CO_2; in these applications, charge carrier dynamics in ambient air plays a significant role.[29-35] Our study is less relevant to photochemical processes taking place in a liquid ambient such as photoelectrochemical water-splitting, photocatalytic water-treatment and dye-sensitized solar cell, however some of the results reported here offer meaningful insights even in such cases particularly when the adsorbed oxygen is involved.

Figure 2a is a schematic illustration of the microwave ring resonator (MRR) and the TiO_2 nanotube array membrane (TNTAM) mounted over the capacitive area while Figure 2b is a photograph of the actual fabricated resonator with the TNTAM in the coupling gap. The normalized electric field strength was found to vary from 100 Vm^{-1} in the blue areas to 5000 Vm^{-1} in the red areas (Figure 2c) using simulations performed in ANSOFT HFSS. These simulations clearly demonstrated the coupling gap and associated capacitance to be the area(s) on the microwave planar resonator that were most sensitive to any variations in the complex permittivity in the vicinity of the resonator. Figure 2d shows the microwave response (transmission coefficient) of the bare resonator and when a titania nanotube membrane is mounted in the coupling gap of the resonator.

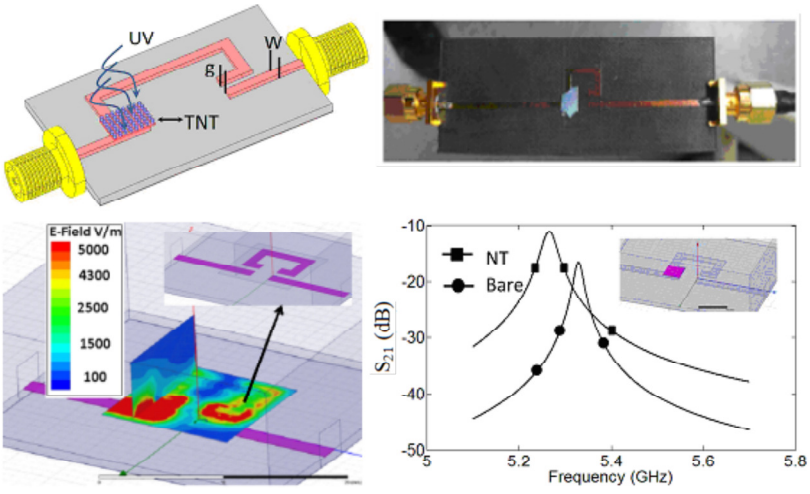

Figure 2. (a) Schematic of the microstrip ring resonator used for simulations (b) Fabricated resonator platform with TiO_2 nanotube array membrane placed in the coupling gap (c) Simulation of the electric field profiles in the resonator showing the highest field intensities occurring in the coupling gap and (d) Change in the ratio of the microwave power transmitted to the output port (S_{21}) and variation of the resonance frequency, quality factor and signal amplitude due to the presence of the TiO_2 nanotube array membrane in the coupling gap.

Experimental Details

The ring resonator was fabricated on a Rogers' substrate (5880) with a dielectric thickness of 0.787 mm, dielectric constant of 2.2 and dissipation factor of 0.0004 and two plated blanket thick films of copper on either side with a thickness of 36 μm. A ring structure with the mentioned specifications for the substrate was designed and simulated in Advanced Design System (ADS) software to operate in the frequency range 5.00−5.50 GHz with a resonance frequency of 5.25 GHz. The main parameters that determine the resonance frequency, are the length and width of the ring line where were designed to be 31 mm for the effective length and 1.5 mm for the width of the lines. Different gap dimensions were investigated to obtain maximum sensitivity, whereupon 1 mm was selected for the width of the coupling gap (g) in this design. The maximum quality factor obtained in simulations for this design was 224 without any nanotube layer. Three-dimensional finite element simulations (using ANSOFT HFSS) on the bare resonator and resonator with TNTAMs in the coupling gap were performed. Electric field distributions over the plate over a 100 μm distance from the surface of the resonator and a vertical cross section of the same area were extracted from the simulations to determine the field enhancement in the sensitive areas as well as the depth of the penetration of the electric field for the simulated structure.

TiO_2 nanotube arrays were formed by electrochemical anodization at room temperature in an ethylene glycol (EG)-based electrolyte containing ammonium fluoride and deionized water, and subsequently delaminated from the Ti foil substrate to form the TNTAMs. As-anodized TNTAMs are amorphous and non-semiconducting. Crystallinity (and concominant semiconducting behavior) was induced by thermal annealing of the membrane at 450°C under flowing oxygen. More details concerning the anodization, delamination and annealing processes may be found in our prior work and elsewhere.[20, 36] Field-emission scanning electron microscopy (FESEM) of the morphology of the TiO_2 nanotube array samples was performed using a Hitachi S-4800 instrument. X-ray diffractograms were collected using a Bruker D8 system. The XRD pattern in Figure 3 provides confirmation that the

TNTAMs were polycrystalline and belonged to the anatase phase. The insets in Fig. 3 are images of the cross-section of the TNTAM showing the self-aligned nanotubular structure. FESEM images indicated the TiO_2 nanotube arrays to have an outer diameter of 150 nm and a tube-length of 160 μm (insets in Fig. 3, also see Figure S1 in Supporting Information).

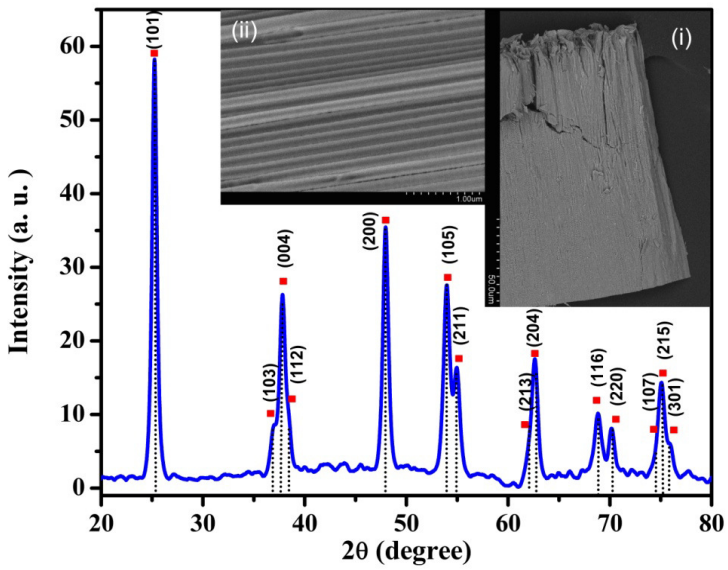

Figure 3. X-ray diffractogram (XRD) of the annealed TiO_2 nanotube array membrane. The indexed peaks confirm the nanotubes to be crystalline and consisting of the anatase phase. Inset (i) shows the cross-sectional SEM image of the entire membrane (scale bar is 5 μm per division) while inset (ii) is a magnified SEM image of the cross-section (scale bar is 100 nm per division).

Results and Discussion

The TNTAMs were mounted on the sample using a small piece of double-sided scotch tape. A baseline measurement was performed with the tape on the substrate and without the TNTAM to justify the source of variation in the resonator's characteristics, which ought to be the TNT membrane alone rather than the substrate or the tape. In this proof-of-concept demonstration of the utility of the MRR to study carrier dynamics, we monitored the recombination behavior of TiO_2 nanotubes at longer time scales of seconds to hours following band gap illumination. In the first experiment, a 254 nm UV lamp illuminated the sample for 20 minutes following which, the variation of the transmitted power (S_{21}) was measured at 10 second intervals (and later at 5 minute intervals subsequent to the first ten minutes) for up to 3 days. This enabled us to study the long-lived component of the decay of the complex photoconductance, which provides insight into trapping states. A second experiment was performed

using the same 254 nm UV lamp and sample but with a cavity waveguide resonator such as shown in Figure 1. The third experiment was the same as the first except that a 365 nm UV source with identical adjusted intensity was used for photoexcitation (Figure 4). A fourth experiment using a 405 nm laser source of identical intensity (0.5 mW cm^2) illuminating the semiconductor with energy just below its band-gap was also conducted. Each of these experiments was repeated several times with the same sample and with other samples as well, and the results were found to be consistent and repeatable.

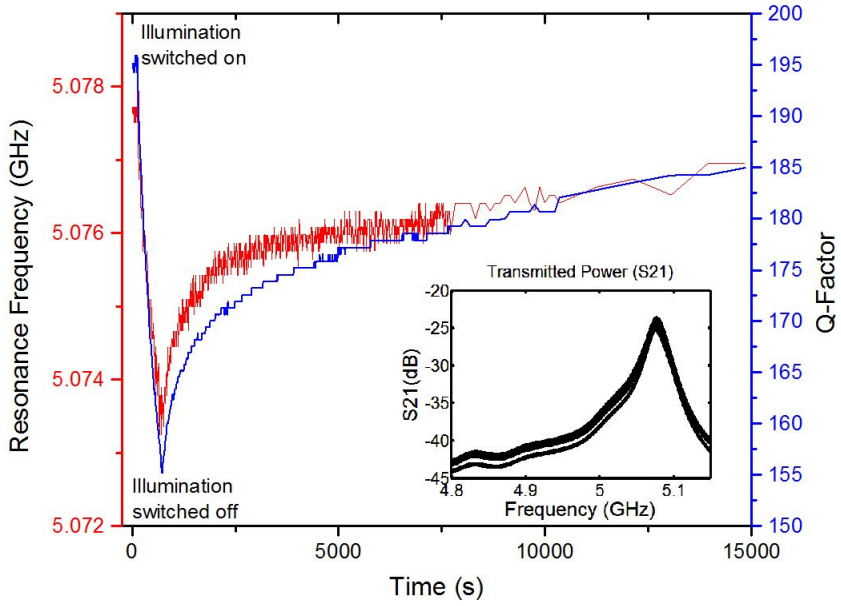

Figure 4. Temporal variation in f_0 and Q following a 2 minute UV illumination from a curing lamp with a centre wavelength of 365 nm at an intensity of 0.5 mW cm^{-2}; (inset) Graph of transmission parameter(S_{21}) for the resonator.

Table 1. Summary of fits and parameters extracted from them*

	Recombination lifetimes and component weights			Indicators of goodness of fits	
Light source and resonator parameter	τ_1 (s)	τ_2 (s)	τ_3 (s)	Reduced χ^2	adj-R^2
254 nm, Q	185.9 (5.2 %)	1403.8 (19.6 %)	21288.1 (75.2 %)	0.053	0.9994
254 nm, f_0	119.3 (8.5 %)	1315.3 (24.3 %)	39499.6 (67.2 %)	> 1	0.9889
365 nm, Q	213.3	1410.2	76589.5	0.097	0.9960

	(0.45 %)	(9.0 %)	(90.5 %)		
405 nm, *Q*	181.8	1852.5	92951.2	0.075	0.9947
	(6.8 %)	(28.2 %)	(65.0 %)		
254 nm, f_0		2014.1	39472.7	> 1	0.9859
(Cavity waveguide)		(8.4 %)	(91.6 %)		
254 nm, *Amplitude*		2846.2	39731.8	0.016	0.9987
(Cavity waveguide)		(2.2 %)	(97.8 %)		

*The recombination lifetimes of trap-mediated processes are not expected to vary as a function of frequency in the range employed. Therefore no significant difference in the microwave response of the TNTAM samples is expected for the 5.5 GHz planar resonator and X-band cavity waveguide.

The complex conductivity (σ) of the TNTAM at a microwave angular frequency ω is given by the Drude model as follows:

$$\sigma_{TNTAM} = \sigma' + j\sigma'' = N_D \frac{e^2}{m^*}\left[\frac{\tau}{1 + j\omega\tau}\right] \qquad (2)$$

where N_D is the equilibrium electron concentration, e is the elementary charge, m^* is the electron effective mass and τ is the momentum relaxation time. The choice of model used affects the relative contributions of trapped and mobile carriers to the complex photoconductance and some recent reports have used either a Drude-Zener or Drude-Smith model to analyze the microwave photoconductance.[37-38] We have stayed with the Drude model since the physical understanding enabled by it is superior and deviations from it are truly important only for terahertz frequencies (0.5-10 THz),[39] where preferential backscattering and plasmon resonance effects become significant and not for the range of frequencies used by us (~ 5.5 GHz). The remaining cause for large deviations from the Drude model at low frequencies is screening-induced depolarization fields due to high photoexcitation densities;[40] this mechanism is not relevant to us either because of our use of relatively weak intensity illumination (~0.5 mW cm-2). Therefore, we used the Drude model in our simulations and calculations.

The penetration depths in the porous TiO_2 nanotube array films for 254 nm, 365 nm and 405 nm radiation were measured by us to be 360 nm, 830 nm and 130 μm respectively. Since the illumination intensity used was identical for the light sources at each of the above three wavelengths, the photoexcited carrier concentration inside the anatase grains constituting the nanotubes is highest when the TNTAMs are illuminated by 254 nm radiation and lowest due to 405 nm radiation - the respective signal strengths for the microwave response following illumination (Figure 4 and Figures S4-S6 in Supporting Information) correlate exactly with the above as expected from absorption coefficient

considerations. Figure 4 and Figures S4-S6 show that 80–250 minutes are required following UV illumination for f_0 and Q to recover to within a few percent of their pre-illumination values. Such a long duration to restore thermal equilibrium is characteristic of thermally-assisted re-emission and recombination processes involving carriers trapped in deep mid-gap states.[41-42] Furthermore, analysis of the microwave response showed that variation in both f_0 and Q both before and after illumination, was dominated by the change in the dielectric constant of TiO_2 nanotubes due to bound charges (photodielectric effect). This is because our circuit modeling and simulations of MRR action demonstrated that f_0 experiences a shift to higher frequencies due to free carriers (positive shift) and a shift to lower frequencies (negative shift) due to bound charges. On the other hand, the loaded Q decreases in either of the above cases due in one case to greater dissipation in a different part of the resonator and due to enhanced free carrier microwave absorption respectively. Consequently, the f_0 data is generally quite noisy while the Q decays are smooth as seen in Figure 4 and Figures S4-S6. Figure 5 shows the complex permittivity of the TNTAM samples extracted by using finite element simulations to fit the experimentally measured S-parameter spectra. The finite element model used estimated the change in the complex permittivity of the entire membrane which would generate the observed shifts in resonance frequency and Q-factor, and is therefore most applicable to the case of the TNTAM illuminated by 405 nm radiation which penetrates through the entire membrane. While the percentage increase in the imaginary part of the permittivity following illumination is larger than in the real part, the absolute magnitude of the imaginary part is significantly smaller than the real part, leading to the dominance of the photodielectric effect over the photoconductive effect in Fig. 4. A triexponential decay described by $Q(\text{or } f_0) = Q_0 + A_1 e^{-t/\tau_1} + A_2 e^{-t/\tau_2} + A_3 e^{-t/\tau_3}$ was found to best fit the recovery curves for Q in Figure 4 for most membranes of high structural integrity and concominant large photoresponse, and consisted of a fast decay component of 120-220 s, a slower decay component of 15-48 min and a third very slow component of 6-26 hours. Membranes with disintegrated or very rough nanotube walls due to rinsing water-induced morphological and phase transformation[43] also showed triexponential decays but with a faster component in the range of ~25 s and the slowest decay component at 2-3 hours. f_0 decays did not possess high goodness of fit likely due to sharp fluctuations and non-monotonic behavior, but a fast component in the range of 160-1000 s and a very long-lived component in the range of hours to days were still evident. A major difference however was that the faster components of the f_0 decay (for 365 nm and 405 nm illumination) were much stronger in weighting than the longer-lived component in opposition to the trends observed in the decays for Q as seen in Table 1. The lifetimes (time constants of the decays) obtained for the cavity waveguide resonator matched well with what we obtained for the

planar resonator (Figure S7 in Supporting Information) except that the cavity waveguide resonator completely missed the fastest component (hence biexponential). This behavior could be due to an un-optimized cavity waveguide design. The results are summarized in Table 1 which shows a good match for τ_2 (s) and τ_3 (s) for both the planar and cavity waveguide setups.

Figure 4 and Figures S4-S7 show that when illumination is present, f_0 experiences purely a negative shift due to the steadily increasing bound charges due to carrier trapping. This does not mean that photogenerated free carriers are not present but that their concentration is much smaller than that of bound charges produced due to illumination (i.e. the bulk of photoexcited electron-hole pairs are trapped). Our results can be explained by the presence of two mid-gap deep trapping levels D_e and D_h, the first closer to the conduction band (CB) edge (and primarily an electron trapping level) and the second closer to the valence band (VB) edge (and primarily a hole trapping level). It is well-known that photogenerated holes in anatase are trapped quickly by deep centers and surface-bound superoxide species, and rendered immobile while CB electrons are relatively stable to recombination with free and trapped holes at temperatures as high as 140 K.[44] Based on this, we assume D_h to be nearly fully occupied during the duration of illumination. Therefore, we assign the initial sharp rise in f_0 and the 120-220 s lifetime component when the illumination is turned off to photogenerated free holes being captured by D_e and thus depopulating electron traps. At this point, free or shallowly trapped electrons begin to be captured by the empty states thus created, resulting in a plateauing of f_0 (due to increase in bound charges) in Figure 4. For 405 nm illumination, even a slight shift back of f_0 toward lower frequencies is seen in Figure S6, manifesting itself as a cusp at ~ 5000 s. The slightly slower component of lifetime 600-2850 s is assigned to this back-filling of depopulated traps by electrons which is also consistent with the high equilibrium density of electrons (both free and in shallow traps) in TiO_2 nanotubes, which has been measured to be 10^{19}-10^{20} cm^{-3}.[45] Our assignment is provided further backing by the observation that the *f0* and *Q* transients during illumination also have a time constant of 300-900 s (not shown) indicating that electron filling of D_e was the rate-limiting step controlling the transient response during illumination. The long-lived component (20000-100000 s) is assigned to thermal re-emission of trapped holes from D_h concominant with fast recombination of re-emitted holes with the large electron population, therefore preserving the monotonicity in *Q* in this time-frame.

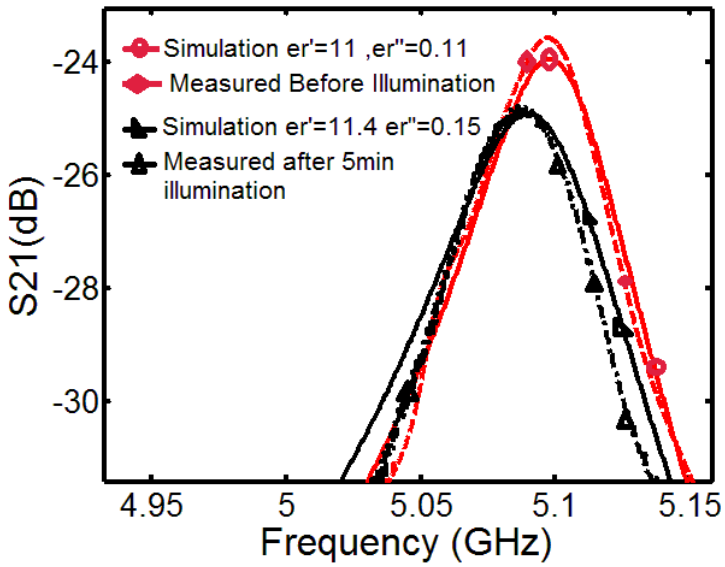

Figure 5. Experimental curves of transmitted power vs. frequency for the TNTAM membranes before (red) and after (black) illumination, compared with simulated fits to the data to obtain the respective complex permittivities.

Oxygen vacancies and adsorbed oxygen atoms are known to produce electron traps and hole traps respectively for photoexcited charge carriers. In organic electrolytes, the anodic growth of TiO_2 nanotubes occurs in oxygen-deficient conditions and while the subsequent crystallization anneal at 500°C restores the stoichiometry of TiO_2, not all oxygen vacancies are filled, particularly inside the nanotube walls. On the surface of *n*-type TiO_2, oxygen atoms from ambient air adsorb and deplete conduction band electrons to form O_2^- ions through the reaction $O_2(g) + e^- \rightarrow O_2^-$.[46] Photoexcited holes are drawn to the surface through the resulting depletion region where they desorb the adsorbed oxygen per the reaction $O_2^- + h^+ \rightarrow O_2(g)$. The radial electric field in the nanotube walls efficiently separates photogenerated electrons and holes, and contributes to a near-complete suppression of geminate recombination. In high surface area materials such as TiO_2 nanotube array membranes, the reactions of photogenerated electrons and holes with molecular oxygen and superoxide anions respectively together constitute the dominant mechanism of carrier relaxation and equilibration. The timescales observed by us through electrodeless measurements for the decay of the complex permittivity of photoexcited TNTAMs are very similar to those measured by others for TNTAMs by electrode-based transient photoconductivity (albeit with applied large signal bias) in ambient air, where such behavior was similarly attributed to interactions with surface-adsorbed oxygen species.[47-49] A question that arises when considering the aforementioned mechanism of oxygen-mediated carrier trapping and

recombination is whether the observed time-constants are descriptive of oxygen adsorption/desorption/diffusion processes or the energetics of deep trap levels. We examined TNTAMs of different structure and thickness, and compared their time constants. Intriguingly, while the magnitude of the resonance frequency shift following illumination varied from 1-50 MHz in different membranes, we found the same set of five time-constants described the decay in all cases and also in a prior report of transient photoconductivity in non-nanostructured polycrystalline anatase films deposited by spray pyrolysis,[50] which would not be the case if the mass transport or surface chemistry were the controlling factors since the surface preparation, effective surface area and porosity would be vastly different for such varied samples. Furthermore, comparisons of the transient photoresponse in ambient air and vacuum have shown oxygen desorption/adsorption processes to take no longer than 200 seconds, and can therefore only explain the fastest component of the decays.[51] This leads us to believe the most or all of the lifetime-components of the microwave photoconductivity decays observed by us are attributable to the times spent by photogenerated electrons and holes in various deep trapping levels. The persistent photoconductivity in TiO_2 upon bandgap illumination was found to be intensity dependent but independent of membrane thickness for TiO_2 nanotubes of length 17 μm - 300 μm. When the illumination intensity for 405 nm radiation was increased from 0.5 mW cm^{-2} to 200 mW cm^{-2}, the decay lifetimes of the resonance frequency shift reduced to 1-5 seconds regardless of membrane thickness, but the amplitude recoveries still exhibited the long-lived lifetimes comparable to those observed at low intensities (see Figure S8). This behavior is a signature of thermally stimulated trap reemission due to heating by the violet laser at high intensities, which reduces the density of shallowly trapped electrons and restores the resonance frequency relatively quickly. On the other hand, the amplitude of the microwave transmission indicative of free carriers takes longer to be restored to the pre-illumination level due to the paucity of direct recombination pathways that are not mediated by deep level traps.

At room temperature, thermally-stimulated trap re-emission is important and the thermal equilibration time for a trap level is given by the time it takes for trap capture and emission processes to achieve equilibrium with each other as in the expression below.

$$\tau_e = \frac{g}{\langle v\sigma \rangle N_v} e^{\frac{E_t - E_v}{kT}} \qquad (2)$$

where g is the trap degeneracy factor (taken to be 2), v is the magnitude of the velocity of free holes (taken to be 3 x 10^6 cm^{-2}),[52] σ is the deep trap capture cross-section (taken to be 10^{-13} cm^{-2} for anatase),[53] N_v is the valence band effective density of states (1.5 x 10^{21} cm^{-3}),[52] E_v is the energy

corresponding to the VB maximum, E_t is the energy level of deep traps, k is Boltzmann's constant and T is the absolute temperature. By applying Equation (2) to the lifetimes we found, we extract a trap-depth of 1.0 to 1.2 eV above the valence band edge, in good agreement with the results from luminescence studies of Mercado et al.[54] In summary, we present the design, simulation, fabrication and proof-of-concept testing of a planar ring microwave resonator-based instrumental configuration to measure microwave conductivity that provides an alternative to the existing cavity waveguide-based set-ups, with several potential benefits. In addition to the electrodeless measurement and microscopic determination of charge transport inherent to all microwave conductivity techniques, the planar resonator design is simple, compact, easy to integrate on printed circuit boards, offers facile fabrication and testing and offers strong interaction of the sample to be probed with microwaves at well-defined spatial locations. The conventional cavity waveguide-based measurement of the microwave properties requires the film to be probed to be grown or deposited on a transparent conducting substrates. This can be a highly limiting restriction for free-standing membranes or films that can only be grown on specific substrates (due to say lattice matching considerations) that in turn may not be transparent or conducting. In a planar ring-type resonator, this restriction is lifted since the film or membrane to be probed merely needs to straddle the mm-sized coupling gap, but a new restriction is introduced which requires the substrate to not be too conductive so as to avoid shorting of the coupling gap. Secondly, the requirement in the cavity waveguide for the sample to be positioned at specific spatial locations to engineer maximum interaction with the microwave radiation (i.e. nodes of the standing wave formed in the waveguide) is also lifted in the planar resonator. Thirdly, planar microwave resonators unlike cavity waveguides allow easy probing of the in-plane and out-of-plane microwave properties by merely mounting the membrane along its base or along its edge, which is a significant advantage for samples that have an anisotropic nanoscale stucture or are made of a material with anisotropic permittivities. Fourthly, monitoring the shift in the resonance frequency and quality factor of the resonator is superior to the mere monitoring of the reflected or transmitted microwave power since richer information on both the amplitude and phase of the microwave signal are obtained. The microwave ring resonator was applied to study the time-resolved microwave photodielectric effect and photoconductivity of TiO_2 nanotube arrays at durations ranging in the minutes to the hours, and allowed extraction of the lifetimes of deep trap-mediated recombination processes occurring at time-scales of seconds to days. An unusual persistence of long-lived charge pairs at room temperature and under ambient conditions was found. While commercially available anatase nanoparticles have shown recombination processes extending to minutes and even hours under vacuum,[55] our observation of the same in TiO_2 nanotubes under ambient conditions is new.

Such a simulation of vacuum behavior may indicate that ambient oxygen and hydroxyl groups are not able to adsorb on to relevant crystal planes in the connected grain structure present in the TNTAMs. Planar resonators also offer considerable flexibility in design and testing that allow the achievement of even higher *Q*-factors, higher photoconductance sensitivity and facile determination of anisotropic complex conductivities (for instance through edge-wise mounting of the membrane in this study).

ASSOCIATED CONTENT

Supporting Information.

Back side of titania nanotube membrane in Fig. S1, Theory of operation of the MRR in Sec. S1, Lumped equivalent circuit models for extraction of sample permittivity in Figs. S2 and S3, Table of fitted lumped model parameters in Table S1 and Fitted photoconductivity decays in Figs. S4-S8. This material is available free of charge via the Internet at http://pubs.acs.org.

AUTHOR INFORMATION

Corresponding author

*Email: kshankar@ualberta.ca.

Notes

The authors declare no competing financial interest.

ACKNOWLEDGEMENTS

This work was made possible by funding support from NSERC, CFI and NRC-NINT. M. D. would like to acknowledge the Canada Research Chair Program. S.F., B.D.W. and A.M. thank Alberta Innovates - Technology Futures for scholarship funding they currently hold or held during a portion of the period in which this research was conducted. The contribution of ECE undergraduates Sam Glassford, Kevin Darraich, Tareq Mosavi and Abdullah Hamid, in the design, simulation, fabrication and testing of X-band cavity waveguide resonators, and that of Ms. Zohreh Poursoti in the growth of select titania nanotube array membranes of different thicknesses, is acknowledged.

REFERENCES

1. De Haas, M. P.; Warman, J. M. Photon-induced molecular charge separation studied by nanosecond time-resolved microwave conductivity. *Chemical Physics* **1982,** *73* (1), 35-53.
2. Martin, S. T.; Herrmann, H.; Choi, W.; Hoffmann, M. R. Time-resolved microwave conductivity. Part 1.—TiO 2 photoreactivity and size quantization. *Journal of the Chemical Society, Faraday Transactions* **1994,** *90* (21), 3315-3322.

3. Martin, S. T.; Herrmann, H.; Hoffmann, M. R. Time-resolved microwave conductivity. Part 2.—Quantum-sized TiO 2 and the effect of adsorbates and light intensity on charge-carrier dynamics. *Journal of the chemical society, Faraday transactions* **1994,** *90* (21), 3323-3330.
4. Dicker, G.; de Haas, M. P.; Siebbeles, L. D.; Warman, J. M. Electrodeless time-resolved microwave conductivity study of charge-carrier photogeneration in regioregular poly (3-hexylthiophene) thin films. *Physical Review B* **2004,** *70* (4), 045203.
5. Meichtry, J. M.; Colbeau-Justin, C.; Custo, G.; Litter, M. I. Preservation of the photocatalytic activity of TiO2 by EDTA in the reductive transformation of Cr(VI). Studies by Time Resolved Microwave Conductivity. *Catal. Today* **2014,** *224*, 236-243.
6. Meichtry, J. M.; Colbeau-Justin, C.; Custo, G.; Litter, M. I. TiO2-photocatalytic transformation of Cr(VI) in the presence of EDTA: Comparison of different commercial photocatalysts and studies by Time Resolved Microwave Conductivity. *Appl. Catal. B-Environ.* **2014,** *144*, 189-195.
7. Talgorn, E.; Moysidou, E.; Abellon, R. D.; Savenije, T. J.; Goossens, A.; Houtepen, A. J.; Siebbeles, L. D. A. Highly Photoconductive CdSe Quantum-Dot Films: Influence of Capping Molecules and Film Preparation Procedure. *The Journal of Physical Chemistry C* **2010,** *114* (8), 3441-3447.
8. Fessenden, R. W.; Carton, P. M.; Shimamori, H.; Scaiano, J. C. Measurement of the dipole moments of excited states and photochemical transients by microwave dielectric absorption. *The Journal of Physical Chemistry* **1982,** *86* (19), 3803-3811.
9. Fessenden, R. W.; Kamat, P. V. Photosensitized charge injection into TiO2 particles as studied by microwave absorption. *Chemical Physics Letters* **1986,** *123* (3), 233-238.
10. Fessenden, R. W.; Kamat, P. V. Rate constants for charge injection from excited sensitizer into SnO2, ZnO, and TiO_2 semiconductor nanocrystallites. *Journal of Physical Chemistry* **1995,** *99* (34), 12902-12906.
11. Donovan, B.; March, N. H. High Frequency Conductivity in Semiconductors. *Proceedings of the Physical Society. Section B* **1956,** *69* (5), 528.
12. Smith, N. V. Classical generalization of the Drude formula for the optical conductivity. *Physical Review B* **2001,** *64* (15), 155106.
13. Kunst, M.; Beck, G. The study of charge carrier kinetics in semiconductors by microwave conductivity measurements. *J. Appl. Phys.* **1986,** *60* (10), 3558-3566.
14. Benedict, T. S.; Shockley, W. Microwave Observation of the Collision Frequency of Electrons in Germanium. *Physical Review* **1953,** *89* (5), 1152-1153.
15. Kopidakis, N. In *Time-Resolved Microwave Conductivity*, Frontiers in Optics 2010/Laser Science XXVI, Rochester, New York, 2010/10/24; Optical Society of America: Rochester, New York, 2010; p LWI4.
16. Jones, A. M.; Kelly, J. F.; Severtsen, R. H.; McCloy, J. S. Regenerative feedback resonant circuit to detect transient changes in electromagnetic properties of semi-insulating materials. *Review of Scientific Instruments* **2013,** *84* (8), -.
17. Perticaroli, S.; Varlamava, V.; Palma, F. Microwave sensing of nanostructured semiconductor surfaces. *Applied Physics Letters* **2014,** *104* (1), -.
18. Zarifi, M.; Sohrabi, A.; Mojir Shaibani, P.; Daneshmand, M.; Thundat, T. Detection of volatile organic compounds using microwave sensors. *Sensors Journal, IEEE* **2014,** *PP* (99), 1-1.
19. Zhang, X.; Han, F.; Shi, B.; Farsinezhad, S.; Dechaine, G. P.; Shankar, K. Photocatalytic Conversion of Diluted CO2 into Light Hydrocarbons Using Periodically Modulated Multiwalled Nanotube Arrays. *Angewandte Chemie* **2012,** *124* (51), 12904-12907.
20. Albu, S. P.; Ghicov, A.; Macak, J. M.; Hahn, R.; Schmuki, P. Self-organized, free-standing TiO2 nanotube membrane for flow-through photocatalytic applications. *Nano Letters* **2007,** *7* (5), 1286-1289.
21. Varghese, O. K.; Paulose, M.; Grimes, C. A. Long vertically aligned titania nanotubes on transparent conducting oxide for highly efficient solar cells. *Nat Nano* **2009,** *4* (9), 592-597.

22. Chen, D.; Zhang, H.; Li, X.; Li, J. Biofunctional Titania Nanotubes for Visible-Light-Activated Photoelectrochemical Biosensing. *Analytical Chemistry* **2010,** *82* (6), 2253-2261.
23. Yoriya, S.; Prakasam, H. E.; Varghese, O. K.; Shankar, K.; Paulose, M.; Mor, G. K.; Latempa, T. J.; Grimes, C. A. Initial Studies on the Hydrogen Gas Sensing Properties of Highly-Ordered High Aspect Ratio TiO2 Nanotube-Arrays 20 um to 222 um in Length. *Sensor Letters* **2006,** *4* (3), 334-339.
24. Mercado, C. C.; Knorr, F. J.; McHale, J. L. Observation of Charge Transport in Single Titanium Dioxide Nanotubes by Micro-Photoluminescence Imaging and Spectroscopy. *ACS Nano* **2012,** *6* (8), 7270-7280.
25. Mohammadpour, R.; Iraji zad, A.; Hagfeldt, A.; Boschloo, G. Comparison of Trap-state Distribution and Carrier Transport in Nanotubular and Nanoparticulate TiO2 Electrodes for Dye-Sensitized Solar Cells. *ChemPhysChem* **2010,** *11* (10), 2140-2145.
26. Zhang, Q.; Celorrio, V.; Bradley, K.; Eisner, F.; Cherns, D.; Yan, W.; Fermín, D. J. Density of Deep Trap States in Oriented TiO2 Nanotube Arrays. *The Journal of Physical Chemistry C* **2014,** *118* (31), 18207-18213.
27. Jennings, J. R.; Ghicov, A.; Peter, L. M.; Schmuki, P.; Walker, A. B. Dye-Sensitized Solar Cells Based on Oriented TiO2 Nanotube Arrays: Transport, Trapping, and Transfer of Electrons. *Journal of the American Chemical Society* **2008,** *130* (40), 13364-13372.
28. Richter, C.; Schmuttenmaer, C. A. Exciton-like trap states limit electron mobility in TiO2 nanotubes. *Nat Nano* **2010,** *5* (11), 769-772.
29. Zhang, X.; Han, F.; Shi, B.; Farsinezhad, S.; Dechaine, G. P.; Shankar, K. Photocatalytic Conversion of Diluted CO2 into Light Hydrocarbons Using Periodically Modulated Multiwalled Nanotube Arrays. *Angewandte Chemie International Edition* **2012**, n/a-n/a.
30. Mohammadpour, A.; Kar, P.; Wiltshire, B. D.; Askar, A. M.; Shankar, K. Electron Transport, Trapping and Recombination in Anodic TiO2 Nanotube Arrays. *Current Nanoscience* **2015,** *11*, (in press).
31. Lin, S.; Li, D.; Wu, J.; Li, X.; Akbar, S. A selective room temperature formaldehyde gas sensor using TiO 2 nanotube arrays. *Sensors and Actuators B: Chemical* **2011,** *156* (2), 505-509.
32. Rao, B. M.; Roy, S. C. Water assisted crystallization, gas sensing and photo-electrochemical properties of electrochemically synthesized TiO 2 nanotube arrays. *RSC Advances* **2014,** *4* (90), 49108-49114.
33. Enachi, M.; Lupan, O.; Braniste, T.; Sarua, A.; Chow, L.; Mishra, Y. K.; Gedamu, D.; Adelung, R.; Tiginyanu, I. Integration of individual TiO2 nanotube on the chip: Nanodevice for hydrogen sensing. *physica status solidi (RRL) – Rapid Research Letters* **2015,** *9* (3), 171-174.
34. Varghese, O. K.; Paulose, M.; LaTempa, T. J.; Grimes, C. A. High-rate solar photocatalytic conversion of CO2 and water vapor to hydrocarbon fuels. *Nano letters* **2009,** *9* (2), 731-737.
35. Ying, Z.; Hoivik, N.; Kaiying, W. In *Photoconductivity of Au-coated TiO_2 nanotube arrays*, Nanotechnology (IEEE-NANO), 2014 IEEE 14th International Conference on, 18-21 Aug. 2014; 2014; pp 180-183.
36. Liu, G. H.; Wang, K. Y.; Hoivik, N.; Jakobsen, H. Progress on free-standing and flow-through TiO2 nanotube membranes. *Sol. Energy Mater. Sol. Cells* **2012,** *98*, 24-38.
37. Dunn, H. K.; Peter, L. M.; Bingham, S. J.; Maluta, E.; Walker, A. B. In Situ Detection of Free and Trapped Electrons in Dye-Sensitized Solar Cells by Photo-Induced Microwave Reflectance Measurements. *The Journal of Physical Chemistry C* **2012,** *116* (41), 22063-22072.
38. Fravventura, M. C.; Deligiannis, D.; Schins, J. M.; Siebbeles, L. D. A.; Savenije, T. J. What Limits Photoconductance in Anatase TiO2 Nanostructures? A Real and Imaginary Microwave Conductance Study. *The Journal of Physical Chemistry C* **2013,** *117* (16), 8032-8040.
39. Shimakawa, K.; Itoh, T.; Naito, H.; Kasap, S. O. The origin of non-Drude terahertz conductivity in nanomaterials. *Applied Physics Letters* **2012,** *100* (13), 132102.

40. Zajac, V.; Němec, H.; Kadlec, C.; Kůsová, K.; Pelant, I.; Kužel, P. THz photoconductivity in light-emitting surface-oxidized Si nanocrystals: the role of large particles. *New Journal of Physics* **2014,** *16* (9), 093013.
41. Lampert, M.; Mark, P. Charge injection in solids. *Academic, New York* **1970**.
42. Studenikin, S. A.; Golego, N.; Cocivera, M. Density of band-gap traps in polycrystalline films from photoconductivity transients using an improved Laplace transform method. *Journal of Applied Physics* **1998,** *84* (9), 5001-5004.
43. Wang, D.; Liu, L.; Zhang, F.; Tao, K.; Pippel, E.; Domen, K. Spontaneous Phase and Morphology Transformations of Anodized Titania Nanotubes Induced by Water at Room Temperature. *Nano Letters* **2011,** *11* (9), 3649-3655.
44. Berger, T.; Sterrer, M.; Diwald, O.; Knözinger, E.; Panayotov, D.; Thompson, T. L.; Yates, J. T. Light-induced charge separation in anatase TiO2 particles. *The Journal of Physical Chemistry B* **2005,** *109* (13), 6061-6068.
45. Pu, P.; Cachet, H.; Ngaboyamahina, E.; Sutter, E. M. M. Relation between morphology and conductivity in TiO2 nanotube arrays: an electrochemical impedance spectrometric investigation. *J Solid State Electrochem* **2013,** *17* (3), 817-828.
46. Anpo, M.; Che, M.; Fubini, B.; Garrone, E.; Giamello, E.; Paganini, M. Generation of superoxide ions at oxide surfaces. *Topics in Catalysis* **1999,** *8* (3-4), 189-198.
47. Cristian, F.; Francisco, H.-R.; Joan Daniel, P.; Román, J.-D.; Teresa, A.; Joan Ramon, M. On the photoconduction properties of low resistivity TiO 2 nanotubes. *Nanotechnology* **2010,** *21* (44), 445703.
48. Zou, J.; Zhang, Q.; Huang, K.; Marzari, N. Ultraviolet Photodetectors Based on Anodic TiO2 Nanotube Arrays. *The Journal of Physical Chemistry C* **2010,** *114* (24), 10725-10729.
49. Liu, G.; Hoivik, N.; Wang, X.; Lu, S.; Wang, K.; Jakobsen, H. Photoconductive, free-standing crystallized TiO2 nanotube membranes. *Electrochimica Acta* **2013,** *93* (0), 80-86.
50. Golego, N.; Studenikin, S. A.; Cocivera, M. Spray pyrolysis preparation of porous polycrystalline thin films of titanium dioxide containing Li and Nb. *Journal of Materials Research* **1999,** *14* (03), 698-707.
51. Golego, N.; Studenikin, S.; Cocivera, M. Effect of oxygen on transient photoconductivity in thin-film Nb x Ti 1-x O 2. *Physical Review B* **2000,** *61* (12), 8262.
52. Le, Z.; Guosheng, S.; Luo, J. K. Numerical study of metal oxide hetero-junction solar cells with defects and interface states. *Semiconductor Science and Technology* **2013,** *28* (5), 055004.
53. Miyagi, T.; Kamei, M.; Mitsuhashi, T.; Yamazaki, A. Superior Schottky electrode of RuO_2 for deep level transient spectroscopy on anatase TiO_2. *Applied Physics Letters* **2003,** *83* (9), 1782-1784.
54. Mercado, C. C.; Knorr, F. J.; McHale, J. L.; Usmani, S. M.; Ichimura, A. S.; Saraf, L. V. Location of Hole and Electron Traps on Nanocrystalline Anatase TiO2. *The Journal of Physical Chemistry C* **2012,** *116* (19), 10796-10804.
55. Szczepankiewicz, S. H.; Moss, J. A.; Hoffmann, M. R. Slow Surface Charge Trapping Kinetics on Irradiated TiO2. *The Journal of Physical Chemistry B* **2002,** *106* (11), 2922-2927.